


Article

General 3D Analytical Method for Eddy-Current Coupling with Halbach Magnet Arrays Based on Magnetic Scalar Potential and H-Functions

Xiaoquan Lu ¹, Xinyi He ², Ping Jin ^{2,*} , Qifeng Huang ¹, Shihai Yang ¹ and Mingming Chen ¹

¹ State Grid Jiangsu Electric Power Co., Ltd., Marketing Service Center, Nanjing 210019, China; seueelab_lxq@163.com (X.L.); hqfyqhqy@126.com (Q.H.); ysh.young@163.com (S.Y.); rd1228@163.com (M.C.)

² The College of Energy and Electrical Engineering, Hohai University, Nanjing 211100, China; hxinyi0927@163.com

* Correspondence: jp81@hhu.edu.cn

Abstract: Rapid and accurate eddy-current calculation is necessary to analyze eddy-current couplings (ECCs). This paper presents a general 3D analytical method for calculating the magnetic field distributions, eddy currents, and torques of ECCs with different Halbach magnet arrays. By using Fourier decomposition, the magnetization components of Halbach magnet arrays are determined. Then, with a group of H-formulations in the conductor region and Laplacian equations with magnetic scalar potential in the others, analytical magnetic field distributions are predicted and verified by 3D finite element models. Based on Ohm's law for moving conductors, eddy-current distributions and torques are obtained at different speeds. Finally, the Halbach magnet arrays with different segments are optimized to enhance the fundamental amplitude and reduce the harmonic contents of air-gap flux densities. The proposed method shows its correctness and validation in analyzing and optimizing ECCs with Halbach magnet arrays.

Keywords: analytical calculation; eddy-current coupling; Halbach magnet array



Citation: Lu, X.; He, X.; Jin, P.; Huang, Q.; Yang, S.; Chen, M. General 3D Analytical Method for Eddy-Current Coupling with Halbach Magnet Arrays Based on Magnetic Scalar Potential and H-Functions. *Energies* **2021**, *14*, 8458. <https://doi.org/10.3390/en14248458>

Academic Editors: Marcin Kamiński and Angel A. Juan

Received: 5 November 2021

Accepted: 9 December 2021

Published: 15 December 2021

Publisher's Note: MDPI stays neutral with regard to jurisdictional claims in published maps and institutional affiliations.



Copyright: © 2021 by the authors. Licensee MDPI, Basel, Switzerland. This article is an open access article distributed under the terms and conditions of the Creative Commons Attribution (CC BY) license (<https://creativecommons.org/licenses/by/4.0/>).

1. Introduction

As a kind of speed-regulating device based on the principle of asynchronous transmission, cylindrical and radial eddy-current couplings (ECCs) with permanent magnets (PMs) have the advantages of high efficiency, energy saving, low maintenance cost, simple installation, and adaptation to harsh environments [1]. Therefore, they can realize power transmission between motor, fan, and pump loads with satisfactory operational characteristics without a mechanical connection [2,3].

A reliable theoretical model for evaluating magnetic field distributions and torque performances is desirable in a PM ECC design. There are three possible approaches to establishing such a model, which is a solution to the moving conductor eddy-current problem. The first approach is to apply numerical methods, such as the finite element method (FEM), which can consider geometric details, the nonlinearity of magnetic materials, and complicated boundary conditions [4]. The 2D FEM is preferred in the early design stage because of time savings [5]. In [6], a radial 2D FEM solver combined with an axial one enables the prediction of the eddy-current paths in three dimensions with the associated losses. The 3D FEM with a Dirichlet boundary condition iteration is introduced to shorten the solving times [7]. In [8], the authors consider the hysteresis behavior of ferromagnetic material by the 3D FEM. However, the calculation of the FEM is time consuming and cannot provide significant relationships between structural parameters and performances [9].

The second approach is the lumped parameter magnetic circuit method (LPMCM), which requires less programming and computing time. An MEC-based analytical method is outlined to calculate a PM ECC's eddy current and reaction flux [10]. In [11], the magnetic field and eddy-current modulations by iron teeth in a conductor disk are considered by

dividing the magnetic flux paths in air gaps into several branches. In [12], the authors calculate an adjustable-speed PM ECC under an asymmetric magnetic field. However, the mentioned LPMCMs can only calculate one PM magnetization direction, namely either the tangential direction or parallel direction, which makes optimization of the magnets impossible [13,14].

As the third approach, the analytical methods derived from simplified boundary conditions and Maxwell's equations are more insightful than the FEM and more accurate than the LPMCM [15–25]. The two most general methods in analytical calculations are magnetic vector potential (MVP) and magnetic scalar potential (MSP). The subdomain technique is used to calculate the 2D magnetic flux density [18]. In [19], the authors calculate the magnetic field distribution of an ECC equipped with disk magnets and high-temperature superconducting pancake coils by assuming an infinite radius of the ferromagnetic yokes. Two-dimensional MSP is also used in an axial field magnetic coupler by assuming the yokes have an infinite radius [20]. In [21,22], 3D MSP is used in the magnet region as well as air gaps for a cylindrical ECC with two-segment Halbach magnets and axial-flux ECCs. In [23], 3D MSP and modified BESSEL functions are used to analyze an air-cored linear and a rotary permanent magnet actuator. In [24], an ECC model directly considers the radial edge effects and the curvature effects on the torque prediction without the need for any correction factor. However, a general analytical analysis with 3D MSP in a cylindrical ECC with Halbach PMs considering the harmonic reduction and optimization has not been presented yet.

This paper presents a 3D analytical analysis of cylindrical ECCs with different Halbach magnet arrays. The coupling analytical models with 3D MSP and H-formulations are established. The magnetization components of four typical Halbach magnet arrays are determined. The magnetic field distributions, eddy currents, torques, fundamental amplitudes, and harmonics of air-gap flux density in different PM arrays are deduced. In addition, the Halbach magnet arrays are optimized to reduce harmonics by selecting the appropriate polar arc coefficient and inclination angle. The 3D simulation and verification are carried out in Cartesian coordinates.

2. Magnetization of Halbach Magnet Arrays

Figure 1 shows the structure of an ECC with a Halbach magnet array. It consists of two rotors: an outer rotor and an inner one. The conductor is on the surface of the former, and the Halbach magnet array is on the latter's surface.

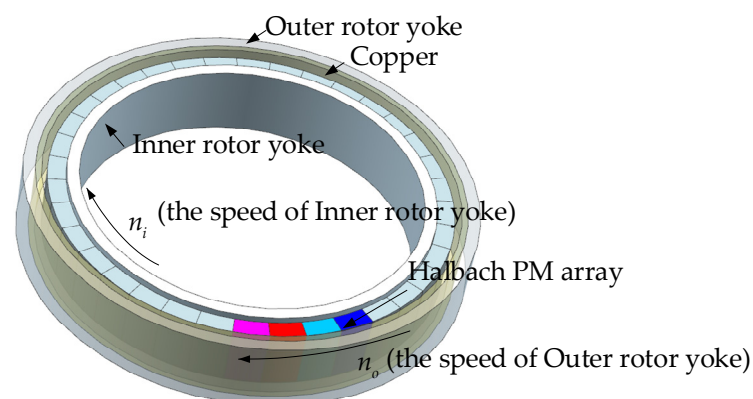


Figure 1. Three-dimensional view of an ECC with Halbach magnet array.

Figure 2a,b show a cylindrical ECC's circumferential and axial cutaways with a three-segment Halbach permanent magnet. The Halbach arrays are distributed along the circumferential direction. The copper is a little longer than the PMs for higher PM utilization rates in the axial direction.

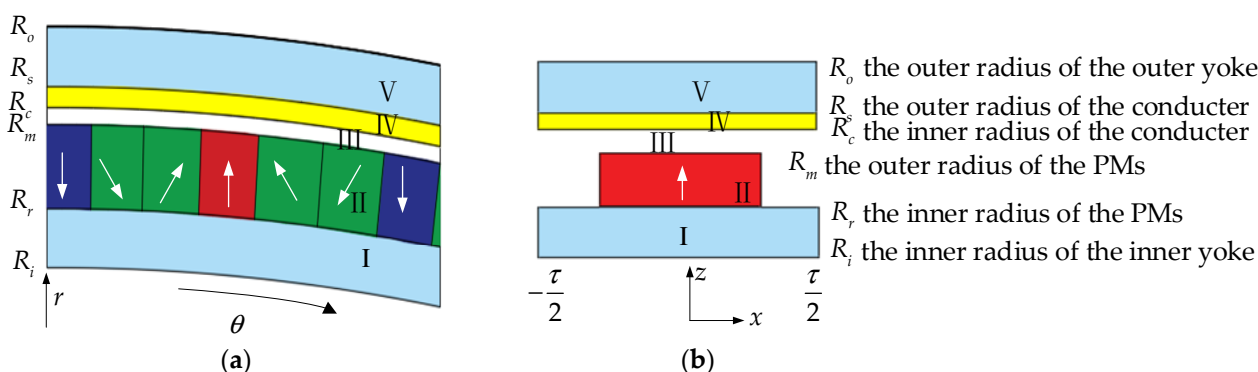


Figure 2. Cutaways of an ECC along the (a) circumferential and (b) axial direction.

The dimensions of a 300 kW cylinder-shaped ECC are $R_i = 309$ mm, $R_r = 324$ mm, $R_m = 350$ mm, $R_c = 356$ mm, $R_s = 362$ mm, $R_o = 380$ mm, $\tau\alpha_r = 60$ mm, $\tau = 100$ mm, $h = 100$ mm, and $l = 85$ mm.

The divided regions are listed in Table 1.

Table 1. The divided regions.

Number	Region	Range of z-Direction	Range of x-Direction
I	Inner yoke region	$R_i < z < R_r$	$-\tau/2 < x < \tau/2$
II	PMs region	$R_r < z < R_m$	$-\tau\alpha_r/2 < x < \tau\alpha_r/2$
III	Air-gap region	$R_m < z < R_c$	$-\tau/2 < x < \tau/2$
IV	Conductor region	$R_c < z < R_s$	$-\tau/2 < x < \tau/2$
V	Outer yoke region	$R_s < z < R_o$	$-\tau/2 < x < \tau/2$

As the curvature effect can be ignored [23], a circumferential topology can be substituted by an equivalent linear structure, where $z = r$ and $x = R_m\theta$. Then, the relative speed v_m is given by:

$$v_m = 2\pi(n_o - n_i)R_m/60 \tag{1}$$

For simplification of the analysis, we adopt the following assumptions:

- (1) The relative recoil permeability of the permanent magnet region is $\mu_r = 1$.
- (2) The conductivity of the outer yoke is zero, and the permeability is infinite. The material of the inner yoke is iron, and the relative permeability is μ_{iron} .
- (3) In region IV, the conductivity of copper σ is constant.

The flux density \vec{B} and magnetic field intensity \vec{H} in regions I, II and III, are given by:

$$\begin{cases} \vec{B}_I = \mu_0\mu_{iron}\vec{H}_I \\ \vec{B}_{II} = \mu_0\mu_r\vec{H}_{II} + \mu_0\vec{M} \\ \vec{B}_{III} = \mu_0\vec{H}_{III} \end{cases} \tag{2}$$

By the separate variable method, the residual magnetization vector \vec{M} is decomposed as:

$$\vec{M} = M_x \vec{x} + M_y \vec{y} + M_z \vec{z} \tag{3}$$

The amplitude of \vec{M} can be given by:

$$M = B_r/\mu_0 \tag{4}$$

Generally, different Halbach arrays are employed in industrial applications, as in Figure 3. The authors have analyzed the magnetic fields of those typical topologies based

on 2D magnetic scalar potential [25]. This paper focuses on the 3D analytical analysis of cylindrical ECCs, where the eddy currents are considered. Figure 3 shows the 3D topologies with different Halbach magnet arrays.

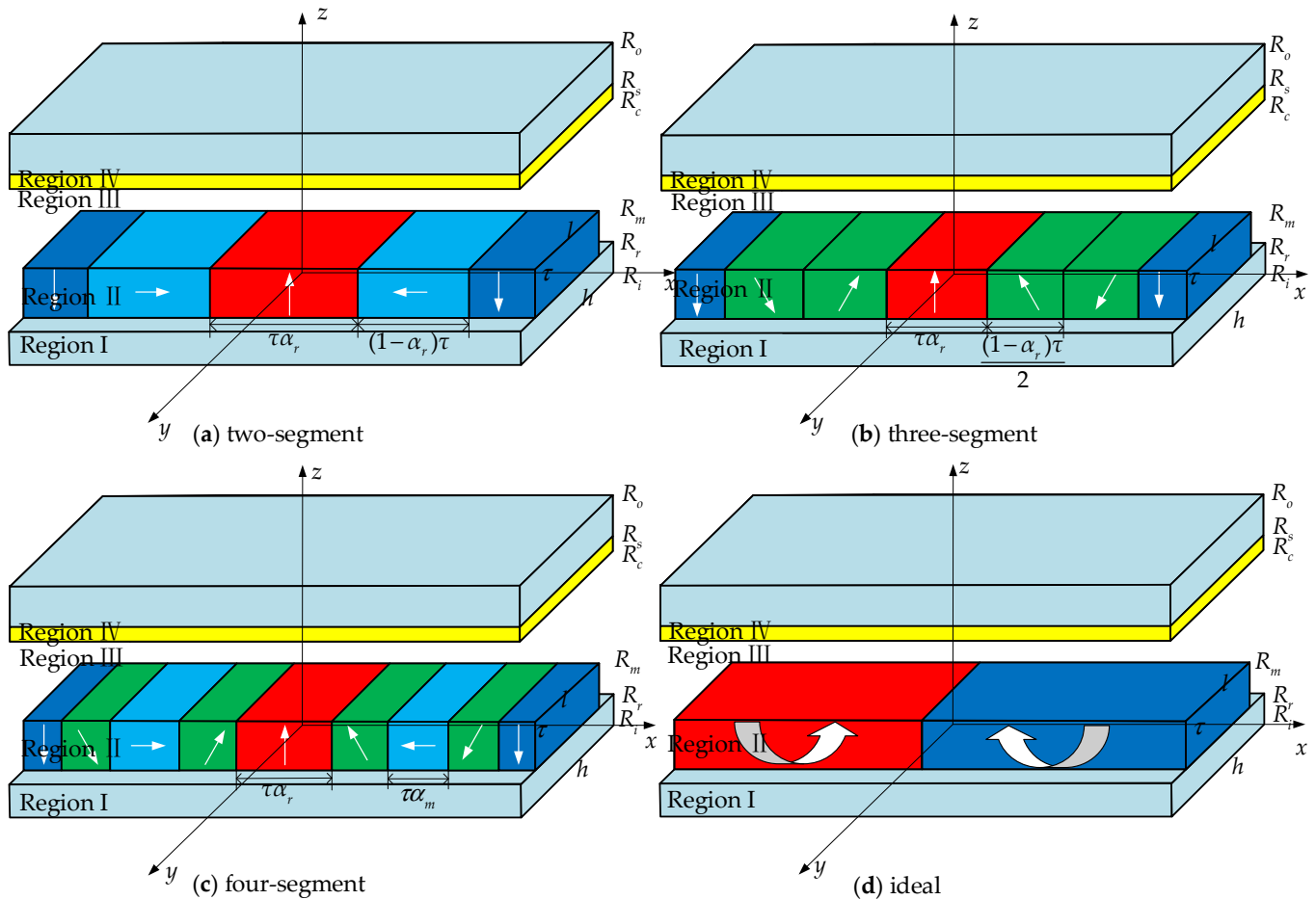


Figure 3. Magnet arrays with different Halbach arrays.

Figure 4 shows the magnetization components of the arrays, where $\delta_x = |\sin\theta|$, $\delta_y = |\cos\theta|$. M_x is an odd function for all four typical Halbach magnet arrays, and M_z is an even function along the x-direction. In the z-direction, as the relative velocity is zero, all regions are extended periodically by the imaging method, and M_z is a homogeneous harmonic even function, as shown in Figure 4e.

By utilizing the Fourier series method, M_x and M_z can be expressed by:

$$\begin{cases} M_x = \sum_{n=1,3,5,\dots}^{\infty} \sum_{k=1,3,5,\dots}^{\infty} M_{xkn} \cos\left(\frac{n\pi}{H}y\right) \sin\left(\frac{k\pi}{\tau}x\right) \\ M_z = \sum_{n=1,3,5,\dots}^{\infty} \sum_{k=1,3,5,\dots}^{\infty} M_{zkn} \cos\left(\frac{n\pi}{H}y\right) \cos\left(\frac{k\pi}{\tau}x\right) \end{cases} \quad (5)$$

and:

$$\begin{cases} M_{xkn} = \frac{4B_r}{\mu_0 kn \pi^2} \sin \frac{n\pi\alpha_q}{2} A_{xk} \\ M_{zkn} = \frac{4B_r}{\mu_0 kn \pi^2} \sin \frac{n\pi\alpha_q}{2} A_{zk} \end{cases} \quad (6)$$

A_{xk} and A_{zk} can be given in Equations (7)–(10) within different topologies.

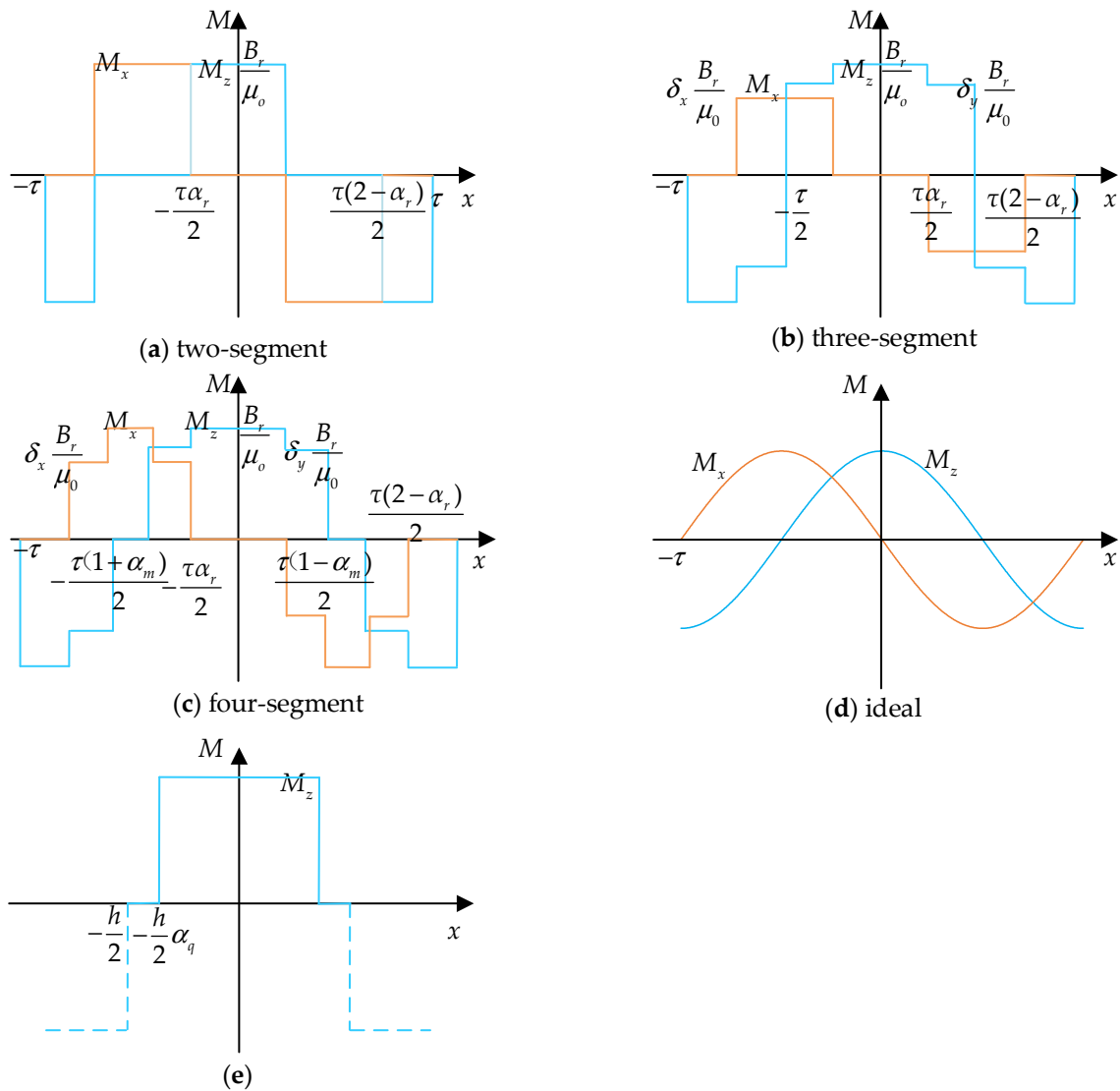


Figure 4. The magnetization components of magnet arrays with different Halbach arrays in (a–d) along the x-direction and (e) along the z-direction.

In the two-segment Halbach array:

$$\begin{cases} A_{xk} = -8 \sin \frac{k\pi(1+\alpha_r)}{2} \sin \frac{k\pi(1-\alpha_r)}{2} \\ A_{zk} = 4 \sin \frac{\pi k \alpha_r}{2} \end{cases} \quad (7)$$

In the three-segment Halbach array:

$$\begin{cases} A_{xk} = -8\delta_x \sin \frac{k\pi(1+\alpha_r)}{4} \sin \frac{k\pi(1-\alpha_r)}{4} \\ A_{zk} = 4 \sin \frac{k\pi \alpha_r}{2} + 8\delta_y \sin \frac{k\pi(1-\alpha_r)}{4} \cos \frac{k\pi(1+\alpha_r)}{4} \end{cases} \quad (8)$$

In the four-segment Halbach array:

$$\begin{cases} A_{xk} = -4 \sin \frac{k\pi}{2} \sin \frac{k\pi\alpha_m}{2} + 4\delta_x (\sin \frac{k\pi}{2} \sin \frac{k\pi\alpha_m}{2} - \cos \frac{k\pi\alpha_r}{2}) \\ A_{zk} = 4 \sin \frac{k\pi \alpha_r}{2} + 4\delta_y (\sin \frac{k\pi}{2} \cos \frac{k\pi \alpha_m}{2} - \sin \frac{k\pi \alpha_r}{2}) \end{cases} \quad (9)$$

In the ideal Halbach array:

$$\begin{cases} A_{xk} = \frac{\sin(1+k)\pi}{1+k} - \frac{\sin(1-k)\pi}{1-k} \\ A_{zk} = \frac{\sin(1+k)\pi}{1+k} + \frac{\sin(1-k)\pi}{1-k} \end{cases} \quad (10)$$

3. Magnetic Field and Eddy-Current Distribution

Since the permeability of an iron core is assumed to be infinite, the Dirichlet boundary condition where $z = R_s$ is satisfied. On both sides of the boundary $z = R_i$, the magnetic field lines are confined mainly in region I. On the boundary $z = R_i$, the Neumann boundary condition can be used approximately. The periodic boundary condition is employed in all directions. Boundary conditions in Figure 2 are given as:

$$\begin{cases} R_s : H_{xIV} = 0 \quad H_{yIV} = 0 \quad \partial H_{zIV} / \partial z = 0 \\ R_c : H_{xIII} = H_{xIV} \quad H_{yIII} = H_{yIV} \quad B_{zIII} = B_{zIV} \\ R_m : H_{xII} = H_{xIII} \quad H_{yII} = H_{yIII} \quad B_{zII} = B_{zIII} \\ R_r : H_{xI} = H_{xII} \quad H_{yI} = H_{yII} \quad B_{zI} = B_{zII} \\ R_i : H_{xI} = 0 \quad H_{yI} = 0 \quad H_{zI} = 0 \end{cases} \quad (11)$$

Solving the partial differential of MSP ϕ_i ($i = I, II, III$), the magnet field intensity components in different regions can be found as

$$H_{xi} = -\frac{\partial \phi_i}{\partial x}, \quad H_{yi} = -\frac{\partial \phi_i}{\partial y}, \quad H_{zi} = -\frac{\partial \phi_i}{\partial z} \quad (12)$$

ϕ_i is expressed by the Laplacian equation as:

$$\frac{\partial^2 \phi_i}{\partial x^2} + \frac{\partial^2 \phi_i}{\partial y^2} + \frac{\partial^2 \phi_i}{\partial z^2} = 0 \quad (13)$$

Then, in regions I and III, the MSP is:

$$\Phi_{I(III)}(x, y) = \text{Re} \left\{ \sum_{k=1}^{\infty} \sum_{n=1}^{\infty} (A_{kn} e^{\gamma z} + B_{kn} e^{-\gamma z}) \cos\left(\frac{k\pi}{H} y\right) e^{j\frac{n\pi}{T} x} \right\} \quad (14)$$

In region II, the general solution is given as:

$$\Phi_{II}(x, y, z) = \text{Re} \left\{ \sum_{k=1}^{\infty} \sum_{n=1}^{\infty} (\bar{C}_{kn} e^{\gamma z} + \bar{D}_{kn} e^{-\gamma z} + \bar{\varphi}) \cos\left(\frac{k\pi}{H} y\right) e^{j\frac{n\pi}{T} x} \right\} \quad (15)$$

In region IV, the time-invariant steady-state is considered. The magnetic field satisfies the static approximation of Maxwell's equations as:

$$\begin{cases} \nabla \cdot B_{IV} = 0 \\ \nabla \times H_{IV} = J_{IV} \\ \nabla \times E_{IV} = -\partial B_{IV} / \partial t = 0 \end{cases} \quad (16)$$

Ohm's law for a moving conductor with reference to the stationary frame is expressed as:

$$J_{IV} = \sigma(E_{IV} + v_m \times B_{IV}) \quad (17)$$

From Equations (16) and (17), the eddy-current problem in region IV is reduced to a magnetostatic problem, which can be solved using an H-formulation as:

$$\nabla^2 H_{IV} = -\sigma \mu_0 \nabla \times (v_m \times H_{IV}) \quad (18)$$

According to the Poisson equation, H_{iIV} ($i = x, y, z$) can be calculated:

$$\frac{\partial^2 H_{iIV}}{\partial x^2} + \frac{\partial^2 H_{iIV}}{\partial y^2} + \frac{\partial^2 H_{iIV}}{\partial z^2} = \sigma \mu_0 V_i \frac{\partial H_{iIV}}{\partial x} \quad (19)$$

By using the method of separation of variables to solve Equations (13) and (19), subject to the distributions of magnetization components and the boundary conditions, general solutions in the four regions are expressed as Equations (20)–(34).

In iron region I:

$$\begin{aligned} H_{xI}(x, y, z) = \text{Re} \left\{ \sum_{k=1}^{\infty} \sum_{n=1}^{\infty} \left(\frac{jn^2 \pi^2}{\gamma^2 \tau^2} M_{xkn} \left(\frac{1}{2} \left(1 + \frac{1}{\mu} \right) \left(-\bar{p} (\sinh \zeta z_d \cosh \gamma (z - z_b - z_c) - \frac{\gamma}{\xi} \cosh \zeta z_d \sinh \gamma (z - z_b - z_c)) + \cosh \gamma (z - z_b) \right) \right. \right. \right. \\ \left. \left. + \frac{1}{2} \left(1 - \frac{1}{\mu} \right) \left(-\bar{p} (\sinh \zeta z_d \cosh \gamma (z + z_b + z_c) + \frac{\gamma}{\xi} \cosh \zeta z_d \sinh \gamma (z + z_b + z_c)) + \cosh \gamma (z + z_b) \right) - \cosh \gamma z \right) \right. \\ \left. + \frac{j k \pi}{\tau \gamma} M_{zkn} \left(\frac{1}{\mu} \sinh \gamma z + \frac{1}{2} \left(1 + \frac{1}{\mu} \right) (\bar{q} (\sinh \zeta z_d \cosh \gamma (z - z_b - z_c) - \frac{\gamma}{\xi} \cosh \zeta z_d \sinh \gamma (z - z_b - z_c) - \sinh \gamma (z - z_b)) \right. \right. \right. \\ \left. \left. + \frac{1}{2} \left(1 - \frac{1}{\mu} \right) (\bar{q} (\sinh \zeta z_d \cosh \gamma (z + z_b + z_c) + \frac{\gamma}{\xi} \cosh \zeta z_d \sinh \gamma (z + z_b + z_c)) + \sinh \gamma (z + z_b)) \right) \right) \cos \left(\frac{k \pi}{H} y \right) e^{j \frac{n \pi x}{\tau}} \right\} \quad (20) \end{aligned}$$

$$\begin{aligned} H_{yI}(x, y, z) = \text{Re} \left\{ \sum_{k=1}^{\infty} \sum_{n=1}^{\infty} \left(-\frac{k n \pi^2}{\gamma^2 \tau H} M_{xkn} \left(\frac{1}{2} \left(1 + \frac{1}{\mu} \right) \left(-\bar{p} (\sinh \zeta z_d \cosh \gamma (z - z_b - z_c) - \frac{\gamma}{\xi} \cosh \zeta z_d \sinh \gamma (z - z_b - z_c)) + \cosh \gamma (z - z_b) \right) \right. \right. \right. \\ \left. \left. + \frac{1}{2} \left(1 - \frac{1}{\mu} \right) \left(-\bar{p} (\sinh \zeta z_d \cosh \gamma (z + z_b + z_c) + \frac{\gamma}{\xi} \cosh \zeta z_d \sinh \gamma (z + z_b + z_c)) + \cosh \gamma (z + z_b) \right) - \cosh \gamma z \right) \right. \\ \left. - \frac{k \pi}{H \gamma} M_{zkn} \left(\frac{1}{\mu} \sinh \gamma z + \frac{1}{2} \left(1 + \frac{1}{\mu} \right) (\bar{q} (\sinh \zeta z_d \cosh \gamma (z - z_b - z_c) - \frac{\gamma}{\xi} \cosh \zeta z_d \sinh \gamma (z - z_b - z_c) - \sinh \gamma (z - z_b)) \right. \right. \right. \\ \left. \left. + \frac{1}{2} \left(1 - \frac{1}{\mu} \right) (\bar{q} (\sinh \zeta z_d \cosh \gamma (z + z_b + z_c) + \frac{\gamma}{\xi} \cosh \zeta z_d \sinh \gamma (z + z_b + z_c)) - \sinh \gamma (z - z_b)) \right) \right) \sin \left(\frac{k \pi}{H} y \right) e^{j \frac{n \pi x}{\tau}} \right\} \quad (21) \end{aligned}$$

$$\begin{aligned} H_{zI}(x, y, z) = \text{Re} \left\{ \sum_{k=1}^{\infty} \sum_{n=1}^{\infty} \left(\frac{n \pi}{\gamma \tau} M_{xkn} \left(\frac{1}{2} \left(1 + \frac{1}{\mu} \right) \left(-\bar{p} (\sinh \zeta z_d \sinh \gamma (z - z_b - z_c) - \frac{\gamma}{\xi} \cosh \zeta z_d \cosh \gamma (z - z_b - z_c)) + \sinh \gamma (z - z_b) \right) \right. \right. \right. \\ \left. \left. + \frac{1}{2} \left(1 - \frac{1}{\mu} \right) \left(-\bar{p} (\sinh \zeta z_d \sinh \gamma (z + z_b + z_c) + \frac{\gamma}{\xi} \cosh \zeta z_d \cosh \gamma (z + z_b + z_c)) + \sinh \gamma (z + z_b) \right) - \sinh \gamma z \right) \right. \\ \left. + M_{zkn} \left(\frac{1}{\mu} \cosh \gamma z + \frac{1}{2} \left(1 + \frac{1}{\mu} \right) (\bar{q} (\sinh \zeta z_d \sinh \gamma (z - z_b - z_c) - \frac{\gamma}{\xi} \cosh \zeta z_d \cosh \gamma (z - z_b - z_c)) - \cosh \gamma (z - z_b) \right) \right. \right. \\ \left. \left. + \frac{1}{2} \left(1 - \frac{1}{\mu} \right) (\bar{q} (\sinh \zeta z_d \sinh \gamma (z + z_b + z_c) + \frac{\gamma}{\xi} \cosh \zeta z_d \cosh \gamma (z + z_b + z_c)) + \cosh \gamma (z + z_b)) \right) \right) \cos \left(\frac{k \pi}{H} y \right) e^{j \frac{n \pi x}{\tau}} \right\} \quad (22) \end{aligned}$$

In PM region II:

$$\begin{aligned} H_{xII}(x, y, z) = \text{Re} \left\{ \sum_{k=1}^{\infty} \sum_{n=1}^{\infty} \left(\frac{j n^2 \pi^2}{\gamma^2 \tau^2} M_{xkn} (\cosh \gamma (z - z_b) - \bar{p} \sinh \zeta z_d \cosh \gamma (z - z_b - z_c) + \bar{p} \frac{\gamma}{\xi} \cosh \zeta z_d \sinh \gamma (z - z_b - z_c) - 1) \right. \right. \\ \left. \left. + \frac{j n \pi}{\gamma \tau} M_{zkn} (-\sinh \gamma (z - z_b) + \bar{q} \sinh \zeta z_d \cosh \gamma (z - z_b - z_c) - \bar{q} \frac{\gamma}{\xi} \cosh \zeta z_d \sinh \gamma (z - z_b - z_c) + 1) \cos \left(\frac{k \pi}{H} y \right) e^{j \frac{n \pi x}{\tau}} \right\} \quad (23) \end{aligned}$$

$$\begin{aligned} H_{yII}(x, y, z) = \text{Re} \left\{ \sum_{k=1}^{\infty} \sum_{n=1}^{\infty} \left(-\frac{n k \pi^2}{\gamma^2 \tau H} M_{xkn} (\cosh \gamma (z - z_b) - \bar{p} \sinh \zeta z_d \cosh \gamma (z - z_b - z_c) + \bar{p} \frac{\gamma}{\xi} \cosh \zeta z_d \sinh \gamma (z - z_b - z_c) - 1) \right. \right. \\ \left. \left. - \frac{k \pi}{\gamma H} M_{zkn} (\bar{q} \sinh \zeta z_d \cosh \gamma (z - z_b - z_c) - \bar{q} \frac{\gamma}{\xi} \cosh \zeta z_d \sinh \gamma (z - z_b - z_c) - \sinh \gamma (z - z_b) + 1) \sin \left(\frac{k \pi}{H} y \right) e^{j \frac{n \pi x}{\tau}} \right\} \quad (24) \end{aligned}$$

$$\begin{aligned} H_{zII}(x, y, z) = \text{Re} \left\{ \sum_{k=1}^{\infty} \sum_{n=1}^{\infty} \left(\frac{n \pi}{\gamma \tau} M_{xkn} (\sinh \gamma (z - z_b) - \bar{p} \sinh \zeta z_d \sinh \gamma (z - z_b - z_c) + \bar{p} \frac{\gamma}{\xi} \cosh \zeta z_d \cosh \gamma (z - z_b - z_c)) \right. \right. \\ \left. \left. + M_{zkn} (-\cosh \gamma (z - z_b) + \bar{q} \sinh \zeta z_d \sinh \gamma (z - z_b - z_c) - \bar{q} \frac{\gamma}{\xi} \cosh \zeta z_d \cosh \gamma (z - z_b - z_c) + 1) \cos \left(\frac{k \pi}{H} y \right) e^{j \frac{n \pi x}{\tau}} \right\} \quad (25) \end{aligned}$$

In air-gap region III:

$$\begin{aligned} H_{xIII}(x, y, z) = \text{Re} \left\{ \sum_{k=1}^{\infty} \sum_{n=1}^{\infty} j \frac{n \pi}{\tau} \frac{1}{\gamma} \left(-\frac{n \pi}{\tau} \frac{1}{\gamma} M_{xkn} \bar{p} + M_{zkn} \bar{q} \right) (\sinh \zeta z_d \cosh \gamma (z - z_b - z_c)) \right. \\ \left. - \frac{\gamma}{\xi} \cosh \zeta z_d \sinh \gamma (z - z_b - z_c) \right) \cos \left(\frac{k \pi}{H} y \right) e^{j \frac{n \pi x}{\tau}} \quad (26) \end{aligned}$$

$$\begin{aligned} H_{yIII}(x, y, z) = \text{Re} \left\{ \sum_{k=1}^{\infty} \sum_{n=1}^{\infty} \left(\left(\frac{n \pi}{\tau \gamma} \right)^2 M_{xkn} \bar{p} - \frac{k \pi}{H \gamma} M_{zkn} \bar{q} \right) (\sinh \zeta z_d \cosh \gamma (z - z_b - z_c)) \right. \\ \left. - \frac{\gamma}{\xi} \cosh \zeta z_d \sinh \gamma (z - z_b - z_c) \right) \sin \left(\frac{k \pi}{H} y \right) e^{j \frac{n \pi x}{\tau}} \quad (27) \end{aligned}$$

$$\begin{aligned} H_{zIII}(x, y, z) = \text{Re} \left\{ \sum_{k=1}^{\infty} \sum_{n=1}^{\infty} \left(-\frac{n \pi}{\tau} \frac{1}{\gamma} M_{xkn} \bar{p} + M_{zkn} \bar{q} \right) (\sinh \zeta z_d \sinh \gamma (z - z_b - z_c)) \right. \\ \left. - \frac{\gamma}{\xi} \cosh \zeta z_d \cosh \gamma (z - z_b - z_c) \right) \cos \left(\frac{k \pi}{H} y \right) e^{j \frac{n \pi x}{\tau}} \quad (28) \end{aligned}$$

In copper region IV:

$$H_{xIV}(x, y, z) = \text{Re} \left\{ \sum_{k=1}^{\infty} \sum_{n=1}^{\infty} \left(j \left(\frac{n \pi}{\tau} \right)^2 \frac{1}{\gamma^2} M_{xkn} \bar{p} - j \frac{k \pi}{\tau} \frac{1}{\gamma} M_{zkn} \bar{q} \right) \sinh \zeta (z_t - z) \cos \left(\frac{k \pi}{H} y \right) e^{j \frac{n \pi x}{\tau}} \right\} \quad (29)$$

$$H_{yIV}(x, y, z) = \text{Re}\left\{ \sum_{k=1}^{\infty} \sum_{n=1}^{\infty} \left(\frac{k\pi}{H} \frac{n\pi}{\tau} \frac{1}{\gamma^2} M_{xkn} \bar{p} + \frac{n\pi}{H} \frac{1}{\gamma} M_{zkn} \bar{q} \right) \sinh \zeta (z_t - z) \sin\left(\frac{k\pi}{H} y\right) e^{j \frac{n\pi}{\tau} x} \right\} \quad (30)$$

$$H_{zIV}(x, y, z) = \text{Re}\left\{ \sum_{k=1}^{\infty} \sum_{n=1}^{\infty} \left(-\frac{1}{\zeta} \frac{n\pi}{\tau} M_{xkn} \bar{p} + \frac{\gamma}{\zeta} M_{zkn} \bar{q} \right) \cosh \zeta (z_t - z) \cos\left(\frac{k\pi}{H} y\right) e^{j \frac{n\pi}{\tau} x} \right\} \quad (31)$$

$$J_{xIV}(x, y, z) = \text{Re}\left\{ \sum_{k=1}^{\infty} \sum_{n=1}^{\infty} \frac{k\pi}{h} M_{zkn} \bar{q} \left(\frac{\zeta}{\gamma} - \frac{\gamma}{\zeta} \right) \cosh(\zeta(z - z_t)) \sin\left(\frac{k\pi}{H} y\right) e^{j \frac{n\pi}{\tau} x} \right\} \quad (32)$$

$$J_{yIV}(x, y, z) = \text{Re}\left\{ \sum_{k=1}^{\infty} \sum_{n=1}^{\infty} j \frac{n\pi}{\tau} M_{zkn} \bar{q} \left(\frac{\zeta}{\gamma} - \frac{\gamma}{\zeta} \right) \cosh(\zeta(z - z_t)) \cos\left(\frac{k\pi}{H} y\right) e^{j \frac{n\pi}{\tau} x} \right\} \quad (33)$$

$$J_{zIV}(x, y, z) = 0 \quad (34)$$

where

$$\begin{aligned} \bar{p} &= [(\sinh \gamma z_a \cosh \gamma z_b - \mu_{iron} \cosh \gamma z_a \sin \gamma z_b) - \sinh \gamma z_a] / q_m, \\ \bar{q} &= [-(\sinh \gamma z_a \sinh \gamma z_b - \mu_{iron} \cosh \gamma z_a \cos \gamma z_b) + \sigma \cosh \gamma z_a] / q_m, \\ q_m &= [\sinh \gamma z_a \cosh \gamma (z_b + z_c) + \mu_{iron} \cosh \gamma z_a \sinh \gamma (z_b + z_c)] \sinh \zeta z_d \\ &\quad + \frac{\gamma}{\zeta} [\sinh \gamma z_a \sinh \gamma (z_b + z_c) + \mu_{iron} \cosh \gamma z_a \cosh \gamma (z_b + z_c)] \cosh \zeta z_d \end{aligned}$$

$$z_a = R_r - R_i, z_b = R_m - R_r, z_c = R_c - R_m, z_d = R_s - R_c, z_t = z_b + z_c + z_d,$$

$$\gamma = \sqrt{\left(\frac{k\pi}{H}\right)^2 + \left(\frac{n\pi}{\tau}\right)^2}, \zeta = \sqrt{\left(\frac{k\pi}{H}\right)^2 + \left(\frac{n\pi}{\tau}\right)^2 + j\sigma\mu_0 V_x \frac{n\pi}{\tau}}$$

By integrating the magnetic field, the electromagnetic torque exerted on the rotor is as follows:

$$T_e = pR_m\mu_0 \int_{-\tau}^{\tau} \int_{-H/2}^{H/2} H_{xIII}(x, y, z_b) H_{yIII}(x, y, z_b) dx dy \quad (35)$$

4. Comparison with the Finite Element Analysis

In order to validate the proposed model, the analytical results are compared with those obtained by the finite element analysis based on three-dimensional (3D) models, using the commercial software package Ansoft Maxwell. The major parameters of the model used in the validation are given in Section 2. The governing equations and boundary conditions in the finite element simulations are:

$$\left\{ \begin{aligned} \nabla \times \frac{1}{\mu_r} \nabla \times A - \nabla \frac{1}{\mu_{iron}} \nabla \cdot A &= \begin{cases} J_{IV} & \text{in region IV} \\ 0 & \text{in region I, III} \\ \nabla \times M & \text{in region II} \end{cases} \\ \left. \begin{aligned} A \times n &= 0 \\ \frac{1}{\mu_{iron}} \nabla \cdot A &= 0 \end{aligned} \right\} S_{\text{boundary}} \end{aligned} \right. \quad (36)$$

In the penalty function, the relative permeability of iron μ_{iron} is defined in Equation (37) to make the coefficient matrix symmetrical.

$$\frac{1}{\mu_{iron}} = \left(\frac{1}{\mu_{ironx}} + \frac{1}{\mu_{irony}} + \frac{1}{\mu_{ironz}} \right) / 3 \quad (37)$$

Considering the structural periodicity of the proposed ECC, only a pair of magnetic poles of this volume is needed to be analyzed. Figure 5a shows the field and grid of the ECC. The mapping mesh with a hexahedron shape is adopted, where the numbers of nodes are 151,040, and elements are 142,506.

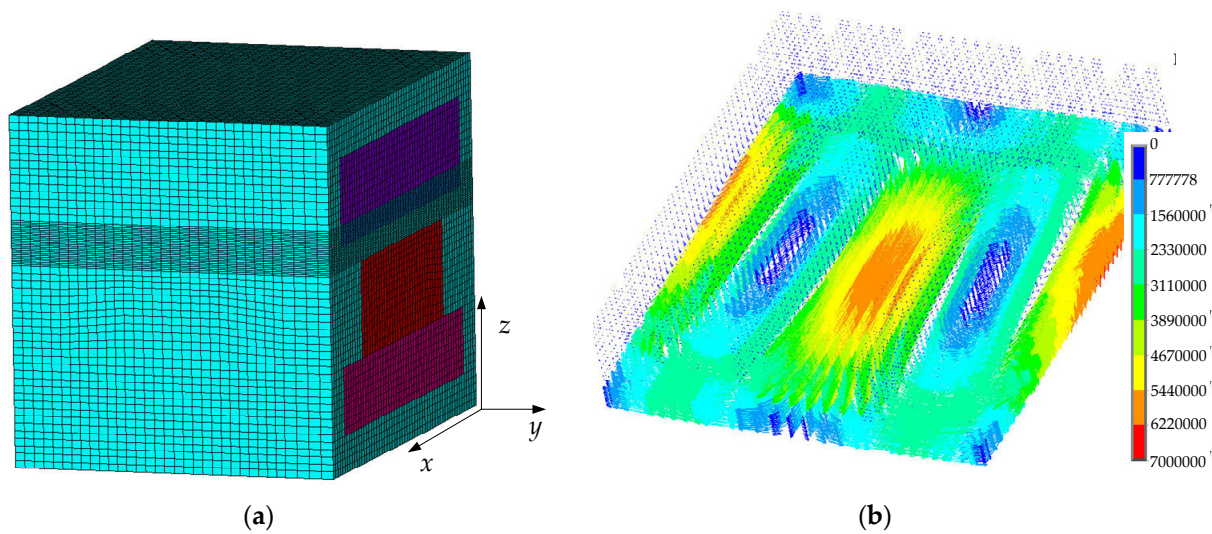


Figure 5. FEM meshes of the solved model (a) and eddy-current distribution of the model (b).

The material's nonlinear properties were considered in the finite element analysis to demonstrate the analytical model's effectiveness and limitations. Since the relative velocity exists in the x-direction, a periodic boundary is used along the direction of motion. Figure 5b shows the eddy-current distribution of the ECC in region IV for a slip speed of 300 rpm.

Figure 6 compares the analytically predicted flux densities and the FEM results of the model shown in Figure 3a in the region IV at $z = R_c + 1/1000$, region III at $z = R_m + 3/1000$, region II at $z = R_m - 1/1000$, and region I at $z = R_r - 1/1000$, respectively. The red line and symbol represent flux densities Br when the slip speed of the ECC is 300 rpm, and the blue line and symbol represent flux densities Bs when the ECC is static.

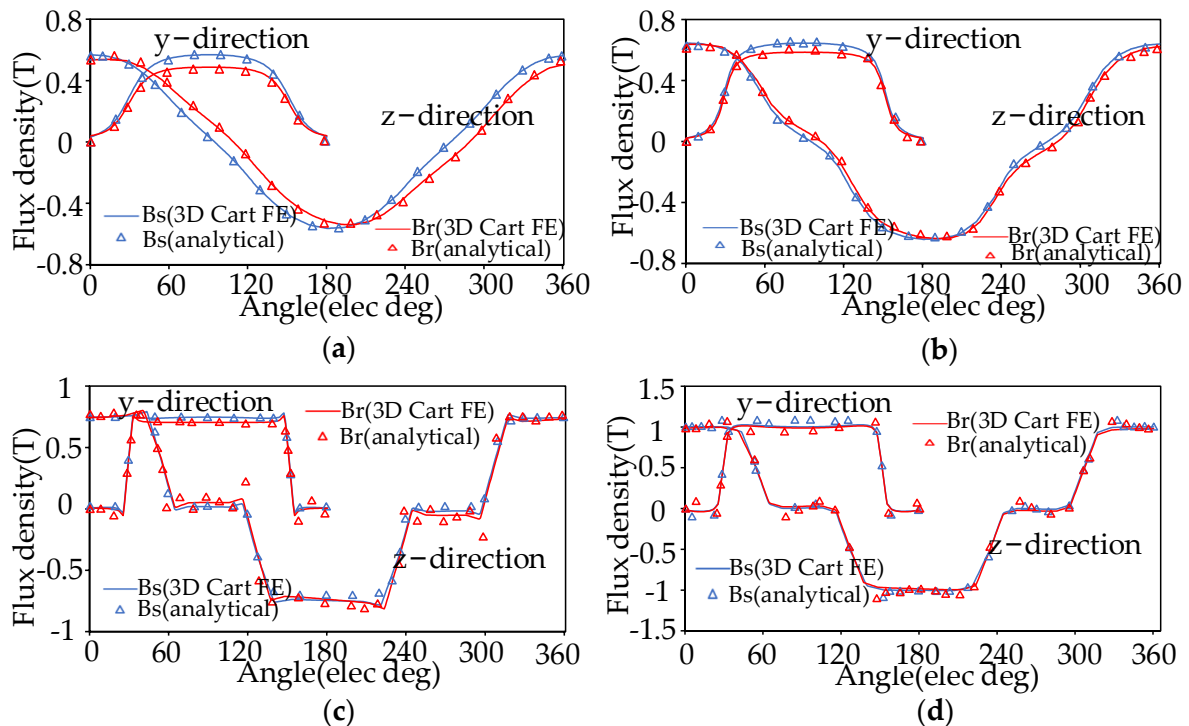


Figure 6. Flux densities in (a) region IV, (b) region III, (c) region II, and (d) region I of the 500 kW ECC with a two-segment Halbach magnet array.

5. Eddy-Current Density Distribution and Torque

Figure 7 presents the eddy-current density distributions along the x-direction in the middle of the copper at $z = R_c + 3/1000$ and $y = 1/2$, obtained by proposed analytical Equations (32)–(34) at different speeds. Figure 8 shows the 3D eddy-current density components at $z = R_c + 3/1000$, in which the x-direction component of the induced current is null at $y = \pm h/2$.

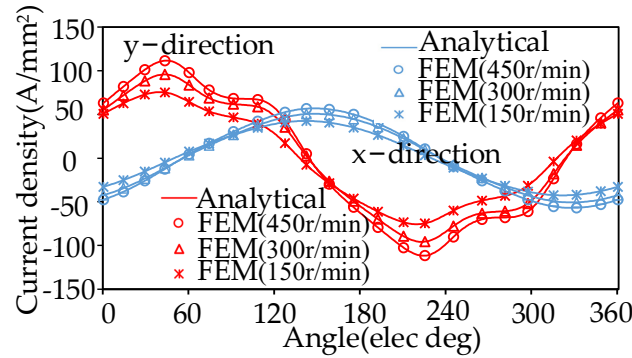


Figure 7. Eddy-current density distributions along the x-direction in the middle of the copper.

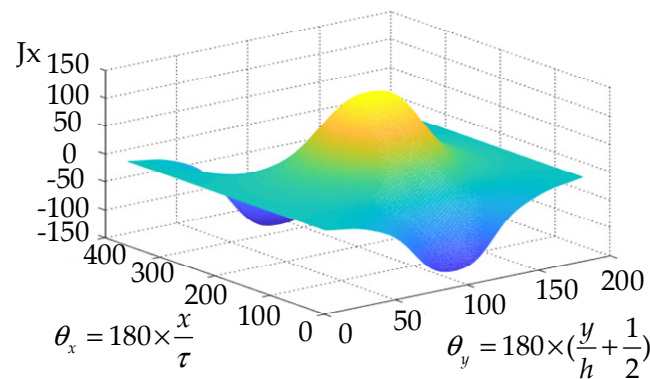


Figure 8. Three-dimensional eddy-current density components distribution in the middle of the copper at 300 rpm.

Figure 9 shows the change in the electromagnetic torque in the analytical method when the slip is changed from 0 to 1 (the rated speed is 1000 rpm). The rated slip and torque of the ECC are 0.02 and 2850 Nm, respectively.

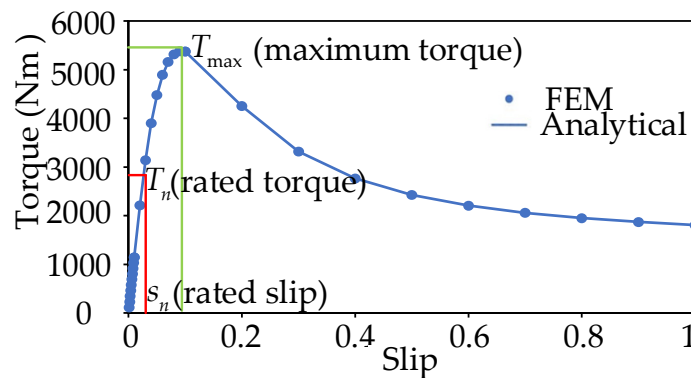


Figure 9. Comparison of the electromagnetic torque by 3D analytical calculation and the FEM.

6. Harmonics and Magnetic Field Optimization

Since there are only odd harmonics of the flux density distribution of the Halbach magnet array in the x and z directions, the harmonics can be easily calculated by the analytical prediction method by taking k and n as odd integers. The amplitude of the air-gap flux density is given by Equation (38), which is obtained from Equation (28) by setting $x = 0$ and $\cos(k\pi y/H) = 1$.

$$F_{(k,n)} = \text{Re}\left\{\sum_{k=1}^{\infty}\sum_{n=1}^{\infty}\left(-\frac{n\pi}{\tau}\frac{1}{\gamma}M_{xkn}\bar{p} + M_{zkn}\bar{q}\right)\left(\sinh\zeta z_d \sinh\gamma(z - z_b - z_c) - \frac{\gamma}{\zeta} \cosh\zeta z_d \cosh\gamma(z - z_b - z_c)\right)\right\} \quad (38)$$

Generally, to reduce cogging torque and speed fluctuation, the air gap magnetic field distribution in ECCs is required to be sinusoidal. The THD of the magnetic field distributions is given by:

$$THD = \sqrt{\sum_{k=2}^{\infty} F_k / F_1} \quad (39)$$

The model shown in Figure 3a was analyzed by an analytical method; Figure 10 shows its variation in the THD and the FA of its flux density in region III when α_r changed from 0 to 1.

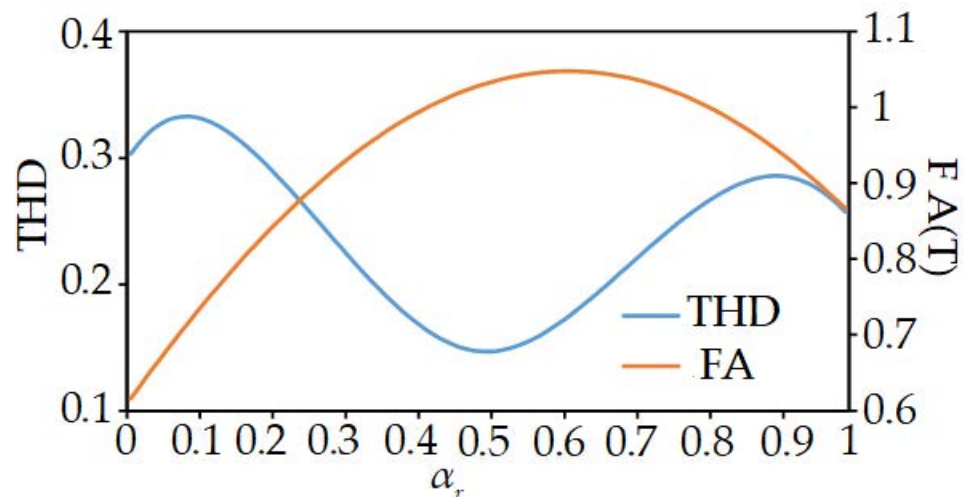


Figure 10. Predicted variation of THD and FA of two-segment Halbach magnet array. α_r represents the x -direction length ratio of the z -direction magnetized PM to τ .

The model shown in Figure 3b was analyzed by the analytical method; Figure 11a shows the contour of the THD and the FA of its flux density in region III when α_r changed from 0 to 1, and θ changed from 0 to 90°. The model shown in Figure 3c was analyzed by the analytical method; Figure 11b shows its contour of the THD and the FA of its flux density in region III when α_r changed from 0 to 1, and θ changed from 0 to 90°.

Taking the model shown in Figure 3b as an example, Table 2 lists the preferred and worst results of the THD and FA. When $\alpha_r = 0.35$ and $\theta = 54^\circ$, the preferred THD is 0.1270, and the preferred FA F_1 is about 1.1051 T. When α_r is changed to zero, and θ is changed to 90°, the FA decreases rapidly.

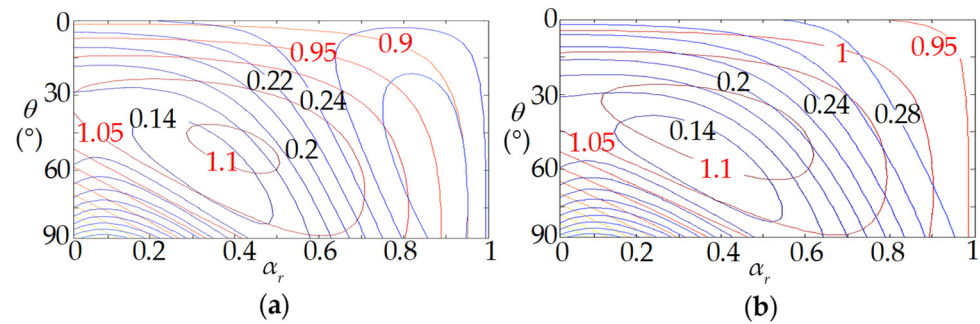


Figure 11. The predicted contours of THD (black numbers) and FA (red numbers) of (a) three-segment and (b) four-segment Halbach magnet array. α_r represents the x-direction length ratio of the z-direction magnetized PM to τ . θ represents the angle of the angular magnetic PM.

Table 2. Preferred and worst results of the three-segment Halbach magnet array.

Item	THD	FA(T)	Position
Non-Halbach	0.2382	0.8574	$\alpha_r = 1$, or $\theta = 0^\circ$
Initial design	0.1408	0.9934	$\alpha_r = 0.33$, $\theta = 45^\circ$
Preferred THD	0.1270	1.0986	$\alpha_r = 0.35$, $\theta = 54^\circ$
Preferred FA	–	1.1051	Preferred Region
Worst THD	0.3327	0.7051	$\alpha_r = 0.04$, $\theta = 90^\circ$
Worst FA	0.3107	0.6290	$\alpha_r = 0$, $\theta = 90^\circ$

Figure 12 compares the flux densities and harmonics of the four Halbach magnet arrays. Figure 12a,b compare the flux densities and harmonics when $\theta = 45^\circ$ and the Halbach arrays are divided into equal parts. Figure 12c,d compare the flux densities and harmonics after optimization. The ideal Halbach magnet array has the smallest harmonic and the largest FA. Figure 13 shows the electromagnetic torques of ECCs with the four Halbach magnetic arrays. The analytical optimization takes less than 10 s to obtain the preferred and worst results, which is much less than the FEM method.

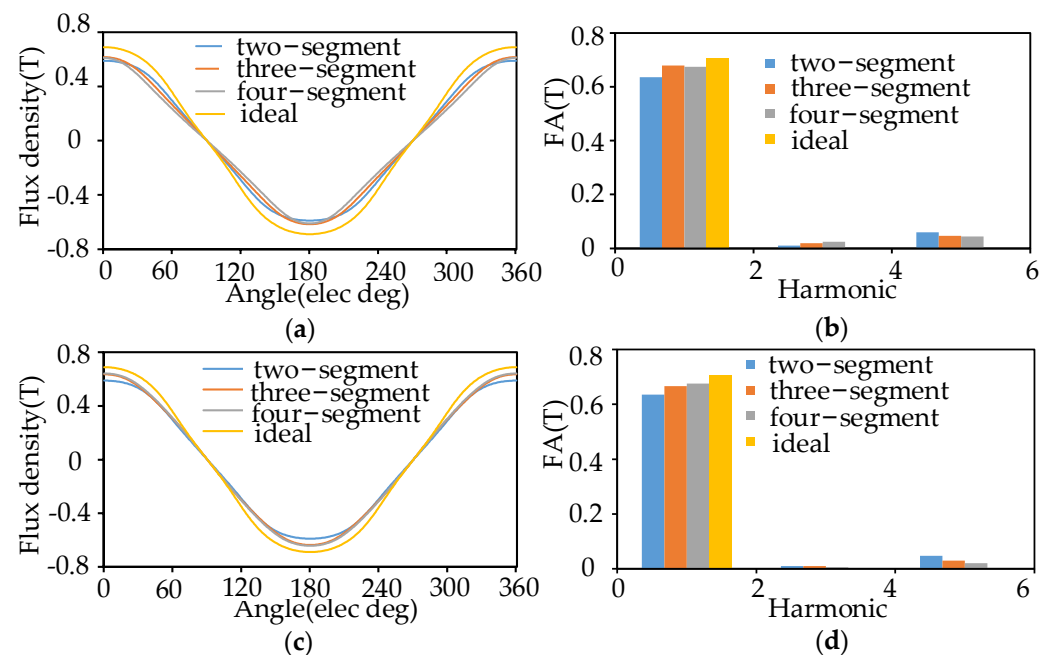


Figure 12. Comparison of flux densities and harmonics when $\theta = 45^\circ$ and Halbach arrays are divided into equal parts in (a,b) and optimal θ and α_r in (c,d).

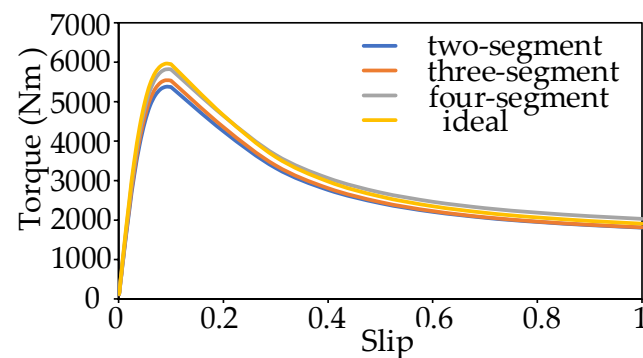


Figure 13. Electromagnetic torques of ECCs with different Halbach magnetic arrays.

7. Conclusions

According to Maxwell's equation, this paper solved the expressions of magnetic field distribution of four typical Halbach arrays. The expressions that have different distribution factors are similar. Three-dimensional analytical magnetic distributions are given using H-formulations in the conductor region and Laplacian equations with magnetic scalar potential in other regions. Eddy currents in the conductor region are obtained from the Ampere law. The results of this method agree with those of the finite element analysis. The comparison verifies the low computational time and good accuracy of the proposed 3D analytical analysis model. The harmonic analysis of the flux densities in the air-gap region is given. Through optimization, the THD of the flux densities decreases, and the amplitude of fundamental waveforms in the air-gap region increases.

The following conclusions can be drawn:

- (1) Based on the 3D analytical analysis, we directly express the 3D flux densities and intensities in the iron region, copper region, PM region, and air-gap region of the typical Halbach topologies and the eddy current in the copper region and the torque of ECCs. All of the analytical results of the flux densities, eddy currents, and torques are verified by the FEM. The proposed analytical model has high precision and efficiency with less calculation time.
- (2) The optimization of the parameters of the typical Halbach topologies is very fast, which can reduce the harmonic of ECC, increase the amplitude of a fundamental wave, and improve the torque efficiently.

Author Contributions: Conceptualization, X.L. and P.J.; methodology, X.L.; software, X.H.; validation, Q.H., S.Y. and M.C.; formal analysis, X.L.; investigation, X.H., Q.H., S.Y. and M.C.; resources, X.L.; data curation, X.L.; writing—original draft preparation, X.L. and X.H.; writing—review and editing, P.J., Q.H., S.Y. and M.C.; visualization, X.H.; supervision, P.J.; project administration, P.J.; funding acquisition, P.J. All authors have read and agreed to the published version of the manuscript.

Funding: This research was funded by NSFC, grant number 51407061.

Institutional Review Board Statement: Not applicable.

Informed Consent Statement: The study did not report any data.

Conflicts of Interest: The authors declare no conflict of interest.

Nomenclature

R_i	The inner radius of the inner yoke
R_r	The inner radius of the permanent magnets
R_m	The outer radius of the permanent magnets
R_c	The inner radius of the conductor
R_s	The outer radius of the conductor
R_o	The outer radius of the outer yoke

$\tau\alpha_r$	Length of the PMs
τ	Length of the yoke (conductor)
n_i	The speeds of the inner rotor
n_o	The speeds of the outer rotor
v_m	The relative velocity of the inner and outer rotor
μ_0	The permeability of the air
μ_r	The relative permeability of the permanent magnet
μ_{iron}	The relative permeability of the iron
B	The flux density scalar
σ	The conductivity of the copper
h	The radial length of the copper
H	The magnet field intensity
l	The radial length of the permanent magnets
M	The residual magnetization of the permanent magnet
$M_x(y,z)$	The x (y, z) direction component of M
ϕ	The magnetic scalar potential
θ	The angle of the angular magnetic permanent magnet
$A_{xk}(zk)$	The kth magnetization distribution factors of the permanent magnet arrays in the x (z) direction
α_r	The x-direction length ratio of the z-direction magnetized PM to τ
α_m	The x-direction length ratio of the x-direction magnetized PM to τ
α_q	The y-direction length ratio of the y-direction magnetized PM to h
E_{IV}	The electric field intensity in the conductor region (region IV)
J_{IV}	The induced current density in the conductor region (region IV)
T_e	The electromagnetic torque
THD	The total harmonic distortion
FA	The amplitude of the flux density
$S_{boundary}$	The outer boundary of the solution domain
$\mu_{ironx}(y,z)$	The x (y, z) direction of the μ_{iron}
A	The magnetic vector potential

References

- Canova, A.; Vusini, B. Design of axial eddy-current couplers. *IEEE Trans. Ind. Appl.* **2003**, *39*, 725–733. [\[CrossRef\]](#)
- Hornreich, R.; Shtrikman, S. Optimal design of synchronous torque couplers. *IEEE Trans. Magn.* **1978**, *14*, 800–802. [\[CrossRef\]](#)
- Furlani, E. Formulas for the force and torque of axial couplings. *IEEE Trans. Magn.* **1993**, *29*, 2295–2301. [\[CrossRef\]](#)
- Grenier, J.-M.; Pérez, R.; Picard, M.; Cros, J. Magnetic FEA direct optimization of high-power density, Halbach array permanent magnet electric motors. *Energies* **2021**, *14*, 5939. [\[CrossRef\]](#)
- Nehl, T.; LeQuesne, B.; Gangla, V.; Gutkowski, S.; Robinson, M.; Sebastian, T. Nonlinear two-dimensional finite element modeling of permanent magnet eddy current couplings and brakes. *IEEE Trans. Magn.* **1994**, *30*, 3000–3003. [\[CrossRef\]](#)
- Stentjes, S.; Boehmer, S.; Hameyer, K. Permanent Magnet Eddy-Current Losses in 2-D FEM Simulations of Electrical Machines. *IEEE Trans. Magn.* **2015**, *51*, 1–4. [\[CrossRef\]](#)
- Aiello, G.; Alfonzetti, S.; Dilettoso, E.; Salerno, N. Eddy Current Computation by the FEM-SDBCI Method. *IEEE Trans. Magn.* **2016**, *52*, 1–4. [\[CrossRef\]](#)
- Fallah, E.; Badeli, V. A New Approach for Modeling of Hysteresis in 2-D Time-Transient Analysis of Eddy Current Using FEM. *IEEE Trans. Magn.* **2017**, *53*, 1–14. [\[CrossRef\]](#)
- Preis, K.; Biro, O.; Tigar, I. FEM analysis of eddy current losses in nonlinear laminated iron cores. *IEEE Trans. Magn.* **2005**, *41*, 1412–1415. [\[CrossRef\]](#)
- Wang, J.; Zhu, J. A Simple Method for Performance Prediction of Permanent Magnet Eddy Current Couplings Using a New Magnetic Equivalent Circuit Model. *IEEE Trans. Ind. Electron.* **2018**, *65*, 2487–2495. [\[CrossRef\]](#)
- Yang, C.; Peng, Z.; Tai, J.; Zhu, L.; Telezing, B.J.K.; Ombolo, P.D. Torque Characteristics Analysis of Slotted-Type Eddy-Current Couplings Using a New Magnetic Equivalent Circuit Model. *IEEE Trans. Magn.* **2020**, *56*, 1–8. [\[CrossRef\]](#)
- Li, Y.; Lin, H.; Yang, H.; Fang, S.; Wang, H. Analytical analysis of a novel flux adjustable permanent magnet eddy-current coupling with a movable stator ring. *IEEE Trans. Magn.* **2018**, *54*, 1–4.
- Li, Y.; Lin, H.; Huang, H.; Yang, H.; Tao, Q.; Fang, S. Analytical Analysis of a Novel Brushless Hybrid Excited Adjustable Speed Eddy Current Coupling. *Energies* **2019**, *12*, 308. [\[CrossRef\]](#)
- Li, B.; Li, G.-D.; Li, H.-F. Magnetic Field Analysis of 3-DOF Permanent Magnetic Spherical Motor Using Magnetic Equivalent Circuit Method. *IEEE Trans. Magn.* **2011**, *47*, 2127–2133. [\[CrossRef\]](#)
- Lubin, T.; Rezzoug, A. Steady-State and Transient Performance of Axial-Field Eddy-Current Coupling. *IEEE Trans. Ind. Electron.* **2015**, *62*, 2287–2296. [\[CrossRef\]](#)

16. Dai, X.; Liang, Q.; Cao, J.; Long, Y.; Mo, J.; Wang, S. Analytical modeling of axial-flux permanent magnet eddy current couplings with a slotted conductor topology. *IEEE Trans. Magn.* **2016**, *52*, 1–15.
17. Min, K.-C.; Choi, J.-Y.; Kim, J.-M.; Cho, H.-W.; Jang, S.-M. Eddy-Current Loss Analysis of Noncontact Magnetic Device With Permanent Magnets Based on Analytical Field Calculations. *IEEE Trans. Magn.* **2015**, *51*, 1–4. [[CrossRef](#)]
18. Akcay, Y.; Giangrande, P.; Tweedy, O.; Galea, M. Fast and Accurate 2D Analytical Subdomain Method for Coaxial Magnetic Coupling Analysis. *Energies* **2021**, *14*, 4656. [[CrossRef](#)]
19. Teymoori, S.; Rahideh, A.; Moayed-Jahromi, H.; Mardaneh, M. 2-D Analytical Magnetic Field Prediction for Consequent-Pole Permanent Magnet Synchronous Machines. *IEEE Trans. Magn.* **2016**, *52*, 1–14. [[CrossRef](#)]
20. Belguerras, L.; Mezani, S.; Lubin, T. Analytical Modeling of an Axial Field Magnetic Coupler With Cylindrical Magnets. *IEEE Trans. Magn.* **2021**, *57*, 1–5. [[CrossRef](#)]
21. Jin, P.; Tian, Y.; Lu, Y.; Guo, Y.; Lei, G.; Zhu, J. 3-D Analytical Magnetic Field Analysis of the Eddy Current Coupling With Halbach Magnets. *IEEE Trans. Magn.* **2020**, *56*, 1–4. [[CrossRef](#)]
22. Lubin, T.; Rezzoug, A. 3-D Analytical Model for Axial-Flux Eddy-Current Couplings and Brakes Under Steady-State Conditions. *IEEE Trans. Magn.* **2015**, *51*, 1–12. [[CrossRef](#)]
23. Jin, P.; Yuan, Y.; Jian, G.; Lin, H.; Fang, S.; Yang, H. Static characteristics of novel air-cored linear and rotary Halbach permanent magnet actuator. *IEEE Trans. Magn.* **2014**, *50*, 977–980. [[CrossRef](#)]
24. Lubin, T.; Rezzoug, A. Improved 3-D Analytical Model for Axial-Flux Eddy-Current Couplings With Curvature Effects. *IEEE Trans. Magn.* **2017**, *53*, 1–9. [[CrossRef](#)]
25. Jin, P.; Yuan, Y.; Lin, H.; Fang, S.; Ho, S.L. General analytical method for magnetic field analysis of Halbach magnet arrays based on magnetic scalar potential. *J. Magn.* **2013**, *18*, 95–104. [[CrossRef](#)]